THE JOURNAL OF PHYSICAL CHEMISTRY C

Article

pubs.acs.org/JPCC

Theoretical Understanding of Enhanced Photoelectrochemical Catalytic Activity of Sn-Doped Hematite: Anisotropic Catalysis and Effects of Morin Transition and Sn Doping

Xiangying Meng,[†,‡] Gaowu Qin,*[,†] William A. Goddard, III,[‡] Song Li,[†] Haijun Pan,[†] Xiaohong Wen,[†] Yaokun Qin,[†] and Liang Zuo[†]

[†]Key Laboratory for Anisotropy and Texture of Materials (MOE), Northeastern University, Shenyang 110819, P. R. China

[‡]Materials and Process Simulation Center, California Institute of Technology, Pasadena, California 91125, United States

ABSTRACT: To investigate the influence of the Morin transition on the photoelectrochemical (PEC) activity of hematite, electronic properties in different magnetic phases were studied on the basis of the first-principles calculations within the GGA+U approximation. The results show that the effective electron mass in the (0001) plane changes remarkably due to the spin−flop transition, while the effective electron masses in other Miller planes are not sensitive to the spin orientation around irons. The electronic structure calculations of Sn-doped hematite predict that the improved PEC activities of Sn-doped hematite are proved to arise from a shrinking of the band gap, decreasing of the effective electron mass, and thus enhanced electronic conductivity. More interestingly, the heavier doping of Sn (≥16.7 atom %) in hematite would induce a new level between the valence band maximum (VBM) and Fermi level E_F, which facilitates its PEC activity of visible light water splitting.

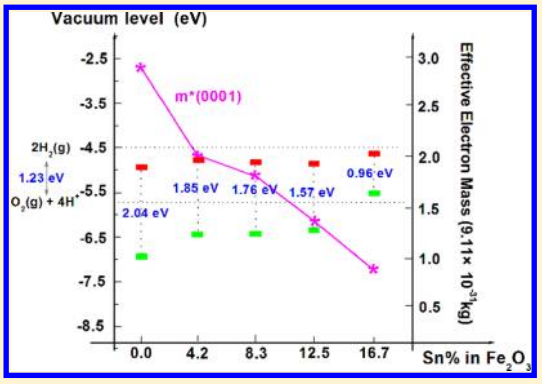

1. INTRODUCTION

The efficient utilization of solar energy is one of the major goals of modern science and engineering.[1,2] Because of its low cost, photocatalytic stability, nontoxicity, and desired narrow indirect band gap of approximately 2.1 eV (which in principle extends the accessibility to the amount of useful solar energy to ∼40%),[3−13] hematite (α-Fe_2O_3) has been paid increasing attention in the last three years for its sustainable and carbon-neutral storage of solar energy by photoelectrochemical (PEC) splitting of water into hydrogen and oxygen.[14−18]

Although hematite exhibits potentially good photocatalytic performance, it suffers from an ultrafast recombination of the photogenerated carriers (time constants on the order of 10 ps).[19−21] To address the problem, many efforts have been devoted to the development of hematite nanostructures and the modification of hematite structure via elemental doping.

An ideal nanostructure increases the photocatalytic performance of hematite, and is always associated with the specific atom arrangement on the surface. Due to a strong anisotropic electronic structure, hematite has been experimentally reported to have a 4 order of magnitude difference in conductivity in different Miller planes.[6,22] However, the determination of an ideal nanosurface giving high photocatalytic efficiency remains elusive.

On the other hand, many elemental doping attempts in hematite have been carried out in past years. Among them, Si,[19,23] Al,[24,25] Mg,[7,26] Zn,[23,25] Mo,[27] Cr,[27] and Ti[24,25,28] were reported to play some roles in improving the PEC activity of hematite. Very recently, Sivula et al. reported a mesoporous hematite photoelectrode prepared by a solution-based colloidal method which yields pronounced water-splitting photocurrents because of the coupling of crystal distortion, particle size, and perhaps Sn diffusion.[11] Subsequently, a series of intentionally Sn-doped hematite nanostructures was synthesized by Li's group.[29] Photoelectrochemical measurements and ultrafast laser spectroscopies were used to confirm that Sn-doped hematite exhibits a superior photocurrent density compared with other dopings. Thus, understanding the mechanism of enhanced photocurrent density in Sn-doped hematite is significant, not only for exploring the reason of improved PEC activity induced by Sn doping but also for the subsequent developing of novel hematite-based photocatalytic materials.

Meanwhile, theoretical studies based on first-principles calculations were, together with the experiments, working toward an understanding of the electronic properties of doped hematite.[22,28,30−32] However, it should be noted that the effect of Morin transition,[33] a spin−flop transition, on the electronic structure has hardly been mentioned in previous attempts of explaining mechanisms or predicting properties of the modified hematite. The experiments are usually performed at a temperature which is higher than the Morin transition temperature of hematite (T_M = −10 °C) and thus samples

Received: October 30, 2012
Revised: January 29, 2013
Published: February 1, 2013

   dx.doi.org/10.1021/jp310740h | J. Phys. Chem. C 2013, 117, 3779−3784

should be weakly ferromagnetic, while the theoretical models used in the density functional theory (DFT) calculations are based on an antiferromagnetic ground state appearing under T_M. Therefore, the DFT results should necessarily be complete and verifiable when applied to predict the photocatalytic performance of real hematite.

To elaborate these points, we report the effective electron masses in different Miller planes of hematite via first-principles electronic structure calculations, based on the magnetic structures found both below and above the Morin transition temperature. The rationality for this work lies in the fact that the effective mass basically determines the capability of carrier transport, including properties from the efficiency of a photocatalyst to the speed of current carriers. Furthermore, the change of effective electron masses in different Miller planes with respect to the gradually increased Sn doping in hematite is also presented. The results are not only helpful to understand the mechanism of enhanced photocurrent density in Sn-doped hematite but also of value in realizing the nature of PEC activities along different crystallographic orientations in the intrinsic hematite and thus developing high catalytic activity structures by surface orientation control.

2. COMPUTATIONAL DETAILS AND MODELS

The geometry optimization and the electronic structure calculations were performed using the VASP[34] code based on the spin-polarized density functional theory. The first-principles pseudopotential approach Perdew–Wang91 was chosen as the exchange-correlation functional. The current calculations made use of an expansion of the electronic wave functions in plane waves with a kinetic-energy cutoff of 600 eV. The total energy was minimized with respect to the volume, the unit shape, and the Wyckoff positions of all atoms. Brillouin-zone integrations were performed using Monkhorst–Pack k-point meshes,[35] and tests were carried out using different k-point meshes to ensure absolute convergence of the total energy with respect to the structural degrees of freedom to a precision of better than 1 meV/atom. In this work, we considered both the localization of the valence states and the mixing of the oxygen p states and iron d states of hematite in the GGA+U framework. This method can deal with delocalized and localized electrons simultaneously, making it particularly effective in the case of hematite because the localized d electrons hybridize significantly with the other orbitals.

The space arrangement of atoms in hematite is presented with a hexagonal cell. In Figure 1, it is clear that the octahedral structural units built by oxygen atoms and centered by iron atoms are slightly rotated against each other. There are two types of pairs of Fe atoms in the lattice, which are characterized by a short Fe–Fe distance and by a larger distance along the hexagonal c-axis. Then, we drew our attention to the need of distinguishing the basic magnetic structures of hematite below and above the Morin temperature. Hematite is experimentally reported having its two magnetic sublattices with the same crystal space structure.[33] We denoted the magnetic structure above T_M as the Morin phase and that below T_M as the zero phase. In the Morin phase, hematite is weakly ferromagnetic because the slight spin canting in the (0001) plane leaves a weak net magnetism along the c-axis. In the zero phase, hematite is antiferromagnetic, the spins around Fe atoms rotate from the basal (0001) plane into alignment along the c-axis, and the net magnetic moment disappears.

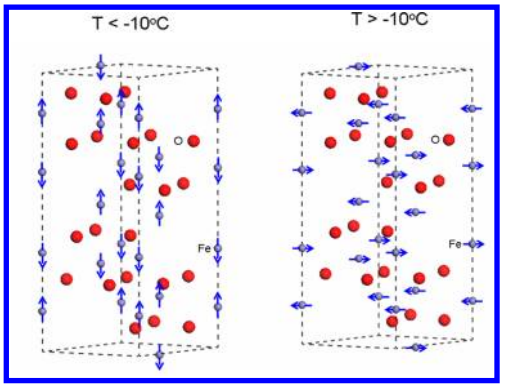

Figure 1. Magnetic order around iron atoms in the hematite hexagonal cell below and above the Morin temperature. The oxygen and iron atoms are indicated with chemical symbol "O" and "Fe", respectively.

Up till this date, the magnetic order in the zero phase has been well determined. In previous work,[28] we also reported the magnetic order for the zero phase in a reduced rhombohedra presentation. In the stable antiferromagnetic ground state, Fe atoms with the short distance (along the hexagonal c-axis) have opposite magnetic moment, while those with the larger distance have equal magnetic moments. The results coincide with LCAO (linear combination of atomic orbital),[36] GGA (generalized gradient approximation),[31] and hybrid density functional theory investigations.[32]

Here we would like to emphasize the representation of stable magnetic order in the Morin phase. To determine the ground magnetic structure, a non-collinear spin polarized method, which has been implemented in VASP code and can be used to manipulate the spin canting, was applied in the first-principles total energy calculations for the different magnetic orders in the Morin phase. The global energy minimum schemes yield a ground magnetic structure which is analogous to that in the zero phase: Fe atoms with the short distance have opposite magnetic moment, while those with the larger distance have equal magnetic moments; the spin component around irons is almost in a–b planes, but a slightly net magnetic moment along the c-axis was found due to the spin canting. After a full relaxation, the value of 6 eV for adjustable U–J parameter yields parameters comparable to experimental values:[37] the magnetization σ_s is 0.01 μ_B, the energy gap is 2.04 eV, and the equilibrium volume is 303.18 Å^3. The total energy of the Morin phase is 0.59 meV per hexagonal cell higher than that of the zero phase.

To simulate Sn-doped hematite, a 120-atom 2 × 2 × 1 supercell was constructed. The Sn atoms were presumed to locate at the highest symmetrical sites to keep the hexagonal lattice and used to substitute for a pair of iron atoms that have opposite magnetic moments, so that experimentally confirmed minimum magnetic moments could be kept by the pair-doping mode. A series of supercells, corresponding to different Sn doping contents of 4.2, 8.3, 12.5, and 16.7 atom %, were sampled. Among the available models for each doping concentration, the cell with the lowest total energy was chosen as the equilibrium structure.

To calculate effective electron mass, we first generated a sequence of reciprocal lattice points k in a given direction and then computed the discrete energy eigenvalues $E_{min}(k)$ for the lowest conduction band for these k-points based on first-principles calculations. By fitting a dispersion relation $E_{min} = f(k)$ at the conduction band minimum (CBM), we can compute

dx.doi.org/10.1021/jp310740h | J. Phys. Chem. C 2013, 117, 3779–3784

the effective electron mass with the definition as $1/m^* = (1/\hbar^2)(d^2E/dk^2)|_{k=k_0}$, where k_0 is the reciprocal lattice point corresponding to the bottom of the conduction band. It is infeasible and unnecessary to investigate the effective electron mass for all Miller planes in hematite. In view of our recent experimental data, which showed a crystallographic texture of hematite nanostructure,[38] we calculated the effective electron mass along the crystallography orientations emerging largely in the XRD samples, for both the Morin and zero phases.

3. RESULTS AND DISCUSSION

First, we investigated the capability of electronic transfer in the intrinsic bulk hematite. The DFT calculated effective electron masses of highly oriented crystal surfaces in the intrinsic bulk hematite are summarized in Table 1. In terms of our results, hematite has a strong anisotropic electrical conductivity and the capability of electronic transfer in pure hematite is rather bad. Generally speaking, the range of effective mass for solid materials is 0.01−10 m_0 (in the unit of ordinary mass of an electron m_0), while the effective electron masses of different crystal surfaces in the intrinsic bulk hematite locate around the maximum value. Therefore, the large effective mass is one of the fundamental unfavorable factors hindering the photocatalytic applications of hematite.

Table 1. Electron Effective Mass in Different Miller Planes (h k i l) for Morin and zero Phases, Presented in the Unit of the Ordinary Mass of an Electron m_o (9.11×10^{-31} kg)

	electron effective mass	
Miller indices (h k i l)	zero	Morin
(0 0 0 1)	8.55 m_o	2.85 m_o
(0 1 $\bar{1}$ 1)	11.76 m_o	11.77 m_o
(0 1 $\bar{1}$ 2)	13.86 m_o	13.86 m_o
(1 0 $\bar{1}$ 4)	10.80 m_o	10.80 m_o
(1 1 $\bar{2}$ 0)	12.88 m_o	12.88 m_o
(1 1 $\bar{2}$ 1)	13.71 m_o	15.23 m_o
(1 1 $\bar{2}$ 3)	15.55 m_o	13.61 m_o
(1 1 $\bar{2}$ 6)	16.06 m_o	21.42 m_o
(2 1 $\bar{3}$ 4)	14.08 m_o	16.09 m_o
(1 0 $\bar{1}$ 0)	16.07 m_o	14.06 m_o

Either in the Morin or zero phase, the order of magnitude of the effective electron mass indicates that the preferred crystal surface possessing relatively higher electrical conductivity is the (0001) plane. It is obvious that the effective electron mass in the (0001) plane is almost 3−6 times lower than that in the other planes when the temperature is above T_M. Since the conductivity is inversely proportional to the effective electron mass, the well-conducting (0001) plane in hematite would collect the photogenerated electrons easier, and also the photogenerated holes can still hop laterally between (0001) planes to reach the electrolyte interface. Thus, the PEC activity of hematite could be improved to some extent by controlling nanostructures with the perfect (0001) texture. To understand this mechanism at the electronic level, a thorough quantum mechanical interpretation of the conductivity anisotropy in hematite[22] has been given through *ab initio* calculations in the context of Marcus theory.[39] In brief, the electronic transfer between adjacent iron double layers is spin-allowed and can proceed, albeit with a higher activation barrier than transfer within the iron planes.[6]

By comparing the effective electron mass in the Morin phase with that in the zero phase, we found that effective electron masses of different Miller planes do not change much except for the (0001) plane. Since the only difference between two phases is the spin directions around iron atoms, it is reasonable to infer that the electronic conductivity, thus the fundamental chemical activity, of hematite is not sensitive to iron's spin orientation. It is the atomic space arrangement and electronic transfer between iron and oxygen atoms that ultimately determine the photocatalytic efficiency of hematite.

The thermodynamic stability of pure and doped hematite in both the Morin and zero phases is investigated by calculations of the cohesive energy E_{coh}, which is defined as the difference between the average energy of the atoms of bulk hematite and that of the isolated atoms. After a full relaxation, the differences in equilibrium volumes ΔV and E_{coh} with respect to the Sn content are listed in Table 2. Compared with experimental parameters ($a = b = 5.035$ Å, $c = 13.750$ Å, $V = 301.90$ Å^3),[40] the present GGA+U calculations lead to an overestimate of 0.42% of the equilibrium volume per hexagonal unit for Morin phase hematite. The variation range of the a-axis is 2.25% and that of the c-axis is 1.75%, which is consistent with the fact that the bonding characters of the Fe−Fe pair bonds are more flexible than the Fe−O rigid octahedral network. In addition, the cohesive energy increases with the increasing Sn concentration, indicating an increased thermodynamic instability with the addition of Sn dopant.

Table 2. The Differences in Equilibrium Volume ΔV (Å^3/Cell) and Cohesive Energy E_{coh} (eV/Atom) Calculated within the GGA+U Approximation for the Pure and Sn-Doped Hematite[a]

	ΔV		E_{coh}	
Sn atom %	zero	Morin	zero	Morin
0.0	0.090	0.000	−2.193	−2.175
4.2	4.948	4.985	−1.776	−1.764
8.3	9.290	9.638	−1.201	−1.183
12.5	14.258	14.295	−0.692	−0.677
16.7	18.665	18.883	−0.116	−0.098

[a]The volume is relative to the equilibrium parameters of the pure hematite in the Morin phase.

The calculated orbital projected density of states (PDOS) of pure hematite for both the Morin and zero phases are plotted in Figure 2, and compared with that of a series of Sn-doped hematite. For pure hematite, the first peak in PDOS is predominated by O-2s bands but with weak Fe-3d states penetrating, which is followed by a narrow band of mainly Fe-3d character, with some admixture with O-2p states and thus a limited Fe−O bonding nature. The upper valence band, lying just below E_F, is essentially of O-2p bonding type with a clear presence of Fe-3d states. A conduction band of Fe-3d character, with a small contribution from O-2p levels giving it a Fe−O bonding nature, is finally observed above E_F. Therefore, the hybridization between O and Fe-3d takes place over the whole band, which is in good agreement with the spectroscopic results.[37,41]

Similar electronic properties are found between the Morin and zero phases when the Sn concentration is lower than 12.5 atom %. Owing to fully filled d-orbitals, there is no Sn-d peak appearing at the band edge closing to the VBM or CBM. The bonding electrons of the Sn dopant belong to 5s and 5p orbitals

dx.doi.org/10.1021/jp310740h | J. Phys. Chem. C 2013, 117, 3779−3784

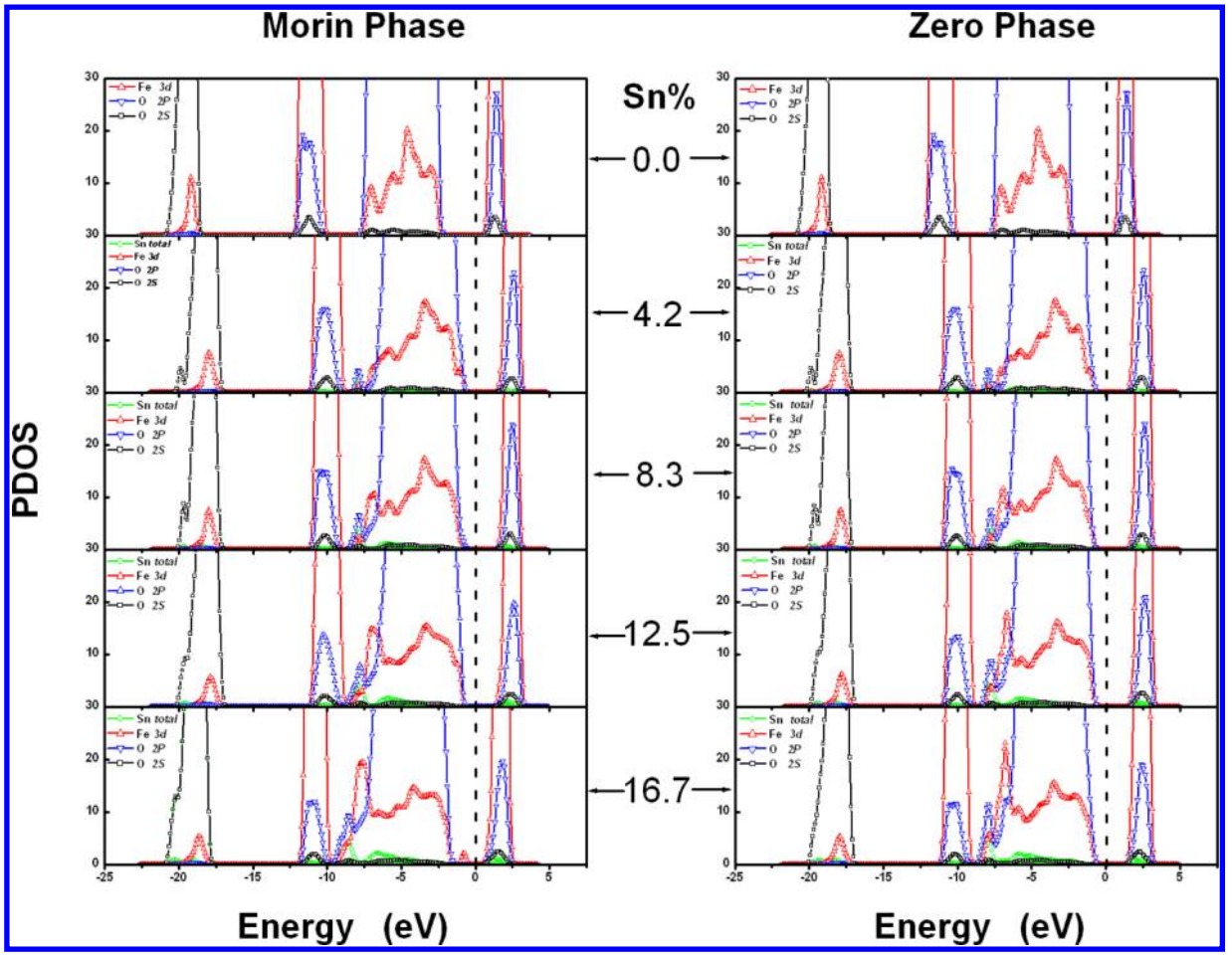

Figure 2. The GGA+*U* calculated PDOS of the Sn-doped hematite compared with that of the pure hematite (for both Morin and zero phases). The Fermi level is set to zero.

and spread in a wide energy range for their nonlocalized properties, which also extend the energy scope of the Fe-3d orbital because of the orbital hybridization. At the same time, the peak intensity of iron and oxygen decreases with increasing electron populations and the lesser number of valence electrons due to the substitution of Sn for Fe atoms.

However, there is a distinct difference in PDOS between the Morin and zero phases when the Sn content increases up to 16.7 atom %. In the Morin phase, a new localized peak of Fe-3d character appears closing to the original valence band maximum, which widens the valence band and induces a remarkable reduction of band gap for heavy doped hematite. Since these newly emerged levels form in the forbidden band, electrons at the valence band edge can absorb photons of a smaller energy to transit easily to these energy levels, and then absorb photons again to jump to conduction bands, which expands the scope of hematite optical absorption. Furthermore, these levels locate between the VBM and the Fermi level E_F and thus are electron-occupied, making themselves effective photoelectron providers instead of electron trappers. These advantages would facilitate the PEC photocurrent density in the Morin phase hematite. However, new peaks are not found between the VBM and CBM in the zero phase based on the present DFT calculations. Therefore, we propose that the heavy Sn doping (atom % $\geq$ 16.5) in the hematite may induce a significant difference in photocatalytic activity between the Morin and zero phases. The further experimental investigations are in progress to verify the theoretical prediction.

To understand the mechanism of high photocurrent density in the Sn-doped hematite, we first pay our attention to the shift of Fermi level E_F. Different from 3d transition metal-doped hematites,[28,30] in which the enhanced photocatalytic activity was mostly owing to the moving of E_F and thereby the increasing number of conductive electrons, E_F does not change the ability of electronic transfer in the Sn-doped hematite because the E_F still locates at the forbidden band. In this regard, the enhanced photocurrent density in the Sn-doped hematite should basically be determined by the reduction of effective electron mass.

To elaborate this point, the calculated VBM, band gap, CBM, and effective electron mass along the hexagonal principal axis versus the increasing concentrations of Sn dopant are plotted in Figure 3. In the energy band picture, the electrical conductivity of an n-type semiconductor is inversely proportional to the electron effective mass at the CBM. It is clear that the electron effective mass at the CBM continued to decrease with increasing Sn content in both the Morin and zero phases, indicating a constantly improved electrical conductivity observed in the Sn-doped hematite.[29] In view of the requirement of photocatalytic applications, such an enhanced electrical conductivity is particularly meritorious because it accelerates the transfer of charge carriers, hinders the recombination of electron−hole pairs, and promotes the

dx.doi.org/10.1021/jp310740h | J. Phys. Chem. C 2013, 117, 3779−3784

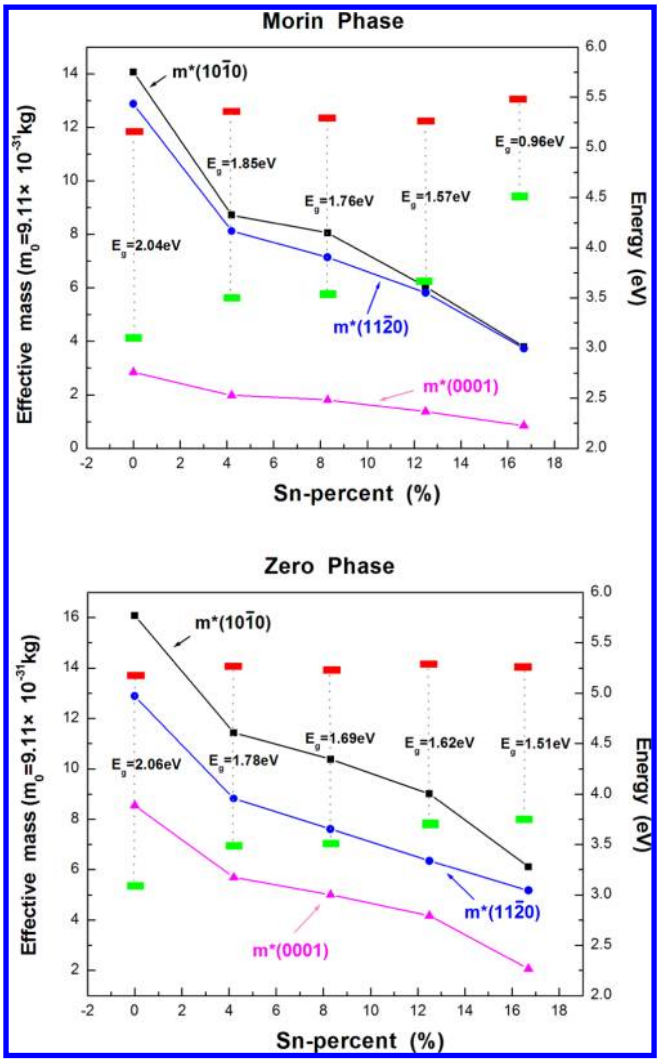

Figure 3. Calculated VBM E_v (indicated by green bar), band gap E_g, CBM E_c (indicated by red bar), and electron effective mass m^* (in the (10$\bar{1}$0), (11$\bar{2}$0), and (0001) planes) versus Sn% for both the Morin and zero phases. E_v, E_g, and E_c are in eV, and referenced to the right; effective electron masses m^* are presented by the ordinary mass of an electron m_o (9.11 × 10^{-31} kg), and referenced to the left.

chance for carriers to participate in the light oxidation–reduction reaction.

In Figure 3, it is clear that the band gap of Sn-doped hematite shrinks gradually with increasing Sn concentration. Thus, a narrower band contributes to improve the utilization of solar radiation. In addition, it is well-known that, for a spontaneous PEC water splitting process, the band edges of the photocatalyst must straddle the water redox potential levels. However, the band alignments of pure hematite can only satisfy the requirement of oxygen production level, while the CBM energy is below the hydrogen production potential.[2] Our calculations show that the CBM of Sn-doped hematite moves up to the hydrogen production level, which is helpful in realizing hydrogen production in visible light driven PEC water splitting.

4. CONCLUSIONS

In summary, we studied the influence of Morin transition on the electronic properties in hematite based on first-principles calculations within the GGA+U framework. The calculated effective electron masses in different Miller planes show that the fundamental photocatalytic activity of hematite is not sensitive to the spin directions around iron atoms, and the theoretical results obtained at the zero phase should not be challenged in most cases. Comparing the magnitude of effective electron masses in different Miller planes, we found that the preferential orientation possessing relatively higher electrical conductivity in hematite is the (0001) plane, and it is thus suggested the PEC activity of hematite can be improved by controlling nanostructures with perfect (0001) texture. Moreover, the effective electron mass of Sn-doped hematite was investigated for both the Morin and zero phases. Sn-doped hematite exhibits an improved electrical conductivity due to the reduction of electron effective mass at the CBM. Heavy Sn doping in hematite can also enhance the utilization ratio of solar energy due to the reduction of band gap and the expansion of optical absorption scope. In the Sn-doped hematite, the shifting of CBM to the hydrogen production level is helpful in achieving hydrogen production in visible light driven PEC water splitting.

AUTHOR INFORMATION

Corresponding Author

*E-mail: qingw@smm.neu.edu.cn.

Notes

The authors declare no competing financial interest.

ACKNOWLEDGMENTS

The authors gratefully acknowledge financial support by National Natural Science Foundation (Nos. 51001025 and 51002026), the Fundamental Research Funds for the Central Universities (Nos. 110810001, 110405003, and N100702001), and National 863 project (2012AA030314). The corresponding author (G.Q.) appreciates the Program for New Century Excellent Talents in University (No. NCET-10-0272).

REFERENCES

(1) Fujishima, A.; Honda, K. Electrochemical Photolysis of Water at a Semiconductor Electrode. *Nature* **1972**, *238*, 37–38.

(2) Grätzel, M. Photoelectrochemical Cells. *Nature* **2001**, *414*, 338–344.

(3) Brillet, J.; Grätzel, M.; Sivula, K. Decoupling Feature Size and Functionality in Solution-Processed, Porous Hematite Electrodes for Solar Water Splitting. *Nano Lett.* **2010**, *10*, 4155–4160.

(4) Frites, M.; Shaban, Y. A.; Khan, S. U. M. Iron Oxide (n-Fe_2O_3) Nanowire Films and Carbon Modified (CM)-n-Fe_2O_3 Thin Films for Hydrogen Production by Photosplitting of Water. *Int. J. Hydrogen Energy* **2010**, *35*, 4944–4948.

(5) Cesar, I.; Kay, A.; Martinez, J. A. G.; Grätzel, M. Translucent Thin Film Fe_2O_3 Photoanodes for Efficient Water Splitting by Sunlight: Nanostructure-Directing Effect of Si-Doping. *J. Am. Chem. Soc.* **2006**, *128*, 4582–4583.

(6) Kay, A.; Cesar, I.; Grätzel, M. New Benchmark for Water Photooxidation by Nanostructured α-Fe_2O_3 Films. *J. Am. Chem. Soc.* **2006**, *128*, 15714–15721.

(7) Gaudon, M.; Pailhe, N.; Majimel, J.; Wattiaux, A.; Abel, J.; Demourgues, A. Influence of Sn^{4+} and Sn^{4+}/Mg^{2+} Doping on Structural Features and Visible Absorption Properties of α-Fe_2O_3 Hematite. *J. Solid State Chem.* **2010**, *183*, 2101–2109.

(8) Hahn, N. T.; Mullins, C. B. Photoelectrochemical Performance of Nanostructured Ti- and Sn-Doped α-Fe_2O_3 Photoanodes. *Chem. Mater.* **2010**, *22*, 6474–6482.

(9) Kumari, S.; Singh, A. P.; Sonal; Deva, D.; Shrivastav, R.; Dass, S.; Satsangi, V. R. Spray Pyrolytically Deposited Nanoporous Ti^{4+} Doped

Hematite Thin Films for Efficient Photoelectrochemical Splitting of Water. *Int. J. Hydrogen Energy* **2010**, *35*, 3985−3990.
(10) Le Formal, F.; Grätzel, M.; Sivula, K. Controlling Photoactivity in Ultrathin Hematite Films for Solar Water-Splitting. *Adv. Funct. Mater.* **2010**, *20*, 1099−1107.
(11) Sivula, K.; Zboril, R.; Le Formal, F.; Robert, R.; Weidenkaff, A.; Tucek, J.; Frydrych, J.; Grätzel, M. Photoelectrochemical Water Splitting with Mesoporous Hematite Prepared by a Solution-Based Colloidal Approach. *J. Am. Chem. Soc.* **2010**, *132*, 7436−7444.
(12) Lin, Y.; S., Z.; Sheehan, S. W.; Wang, D. Nanonet-Based Hematite Heteronanostructures for Efficient Solar Water Splitting. *J. Am. Chem. Soc.* **2011**, *133*, 2398−2401.
(13) Tilley, S. D.; Cornuz, M.; Sivula, K.; Grätzel, M. Light-Induced Water Splitting with Hematite: Improved Nanostructure and Iridium Oxide Catalysis. *Angew. Chem., Int. Ed.* **2010**, *49*, 6405−6408.
(14) Liu, R.; Lin, Y.; Chou, L. Y.; Sheehan, S. W.; He, W.; Zhang, F.; Hou, H. J. M.; Wang, D. Water Splitting by Tungsten Oxide Prepared by Atomic Layer Deposition and Decorated with an Oxygen-Evolving Catalyst. *Angew. Chem., Int. Ed.* **2011**, *50*, 499−502.
(15) Wang, G. M.; Yang, X. Y.; Qian, F.; Zhang, J. Z.; Li, Y. Double-Sided CdS and CdSe Quantum Dot Co-Sensitized ZnO Nanowire Arrays for Photoelectrochemical Hydrogen Generation. *Nano Lett.* **2010**, *10*, 1088−1092.
(16) Hensel, J.; Wang, G.; Li, Y.; Zhang, J. Z. Synergistic Effect of CdSe Quantum Dot Sensitization and Nitrogen Doping of TiO_2 Nanostructures for Photoelectrochemical Solar Hydrogen Generation. *Nano Lett.* **2010**, *10*, 478−483.
(17) Yang, X. Y.; Wolcott, A.; Wang, G. M.; Sobo, A.; Fitzmorris, R. C.; Qian, F.; Zhang, J. Z.; Li, Y. Nitrogen-Doped ZnO Nanowire Arrays for Photoelectrochemical Water Splitting. *Nano Lett.* **2009**, *9*, 2331−2336.
(18) Lin, Y.; Zhou, S.; Liu, X. H.; Sheehan, S. W.; Wang, D. TiO_2/$TiSi_2$ Heterostructures for High-Efficiency Photoelectrochemical H_2O Splitting. *J. Am. Chem. Soc.* **2009**, *131*, 2772−2773.
(19) Cesar, I.; Sivula, K.; Kay, A.; Zboril, R.; Grätzel, M. Influence of Feature Size, Film Thickness, and Silicon Doping on the Performance of Nanostructured Hematite Photoanodes for Solar Water Splitting. *J. Phys. Chem. C* **2009**, *113*, 772−782.
(20) Cherepy, N. J.; Liston, D. B.; Lovejoy, J. A.; Deng, H. M.; Zhang, J. Z. Ultrafast Studies of Photoexcited Electron Dynamics in γ- and α-Fe_2O_3 Semiconductor Nanoparticles. *J. Phys. Chem. B* **1998**, *102*, 770−776.
(21) Dareedwards, M. P.; Goodenough, J. B.; Hamnett, A.; Trevellick, P. R. Electrochemistry and Photoelectrochemistry of Iron(III) Oxide. *J. Chem. Soc., Faraday Trans. 1* **1983**, *79*, 2027−2041.
(22) Iordanova, N.; Dupuis, M.; Rosso, K. M. Charge Transport in Metal Oxides: A Theoretical Study of Hematite α-Fe_2O_3. *J. Chem. Phys.* **2005**, *122*, 144305−144314.
(23) Satsangi, V. R.; Kumari, S.; Singh, A. P.; Shrivastav, R.; Dass, S. Nanostructured Hematite for Photoelectrochemical Generation of Hydrogen. *Int. J. Hydrogen Energy* **2008**, *33*, 312−318.
(24) Glasscock, J. A.; Barnes, P. R. F.; Plumb, I. C.; Savvides, N. Enhancement of Photoelectrochemical Hydrogen Production from Hematite Thin Films by the Introduction of Ti and Si. *J. Phys. Chem. C* **2007**, *111*, 16477−16488.
(25) Sartoretti, C. J.; Alexander, B. D.; Solarska, R.; Rutkowska, W. A.; Augustynski, J.; Cerny, R. Photoelectrochemical Oxidation of Water at Transparent Ferric Oxide Film Electrodes. *J. Phys. Chem. B* **2005**, *109*, 13685−13692.
(26) Ingler, W. B.; Khan, S. U. M. Synthesized Magnesium-Doped Iron (III) Oxide (p-Fe_2O_3) Thin Films under Solar Simulated Light Illumination. *Thin Solid Films* **2004**, *461*, 301−308.
(27) Kleiman-Shwarsctein, A.; Hu, Y. S.; Forman, A. J.; Stucky, G. D.; McFarland, E. W. Electrodeposition of α-Fe_2O_3 Doped with Mo or Cr as Photoanodes for Photocatalytic Water Splitting. *J. Phys. Chem. C* **2008**, *112*, 15900−15907.
(28) Meng, X. Y.; Qin, G. W.; Li, S.; Wen, X. H.; Ren, Y. P.; Pei, W. L.; Zuo, L. Enhanced Photoelectrochemical Activity for Cu and Ti Doped Hematite: The First Principles Calculations. *Appl. Phys. Lett.* **2011**, *98*, 112104−112106.
(29) Ling, Y. C.; Wang, G. M.; Wheeler, D. A.; Zhang, J. Z.; Li, Y. Sn-Doped Hematite Nanostructures for Photoelectrochemical Water Splitting. *Nano Lett.* **2011**, *11*, 2119−2125.
(30) Huda, M. N.; Walsh, A.; Yan, Y. F.; Wei, S. H.; Jassim, M. M. A. Structural, and Magnetic Effects of 3*d* Transition Metals in Hematite. *J. Appl. Phys.* **2010**, *107*, 123712−123718.
(31) Rollmann, G.; Rohrbach, A.; Entel, P.; Hafner, J. First-Principles Calculation of the Structure and Magnetic Phases of Hematite. *Phys. Rev. B* **2004**, *69*, 165107−165119.
(32) Wilson, N. C.; Russo, S. P. Hybrid Density Functional Theory Study of the High-Pressure Polymorphs of α-Fe_2O_3 Hematite. *Phys. Rev. B* **2009**, *79*, 094113−094122.
(33) Morin, F. J. Magnetic Susceptibility Of αFe_2O_3 and αFe_2O_3 with Added Titanium. *Phys. Rev.* **1950**, *78*, 819−820.
(34) Kresse, G.; Furthmuller, J. Efficient Iterative Schemes for *ab Initio* Total-Energy Calculations Using a Plane-Wave Basis Set. *Phys. Rev. B* **1996**, *54*, 11169−11186.
(35) Monkhorst, H. J.; Pack, J. D. Special Points for Brillouin-Zone Integrations. *Phys. Rev. B* **1976**, *13*, 5188−5192.
(36) Catti, M.; Valerio, G. Theoretical Study of Electronic, Magnetic, and Structural Properties of α-Fe_2O_3. *Phys. Rev. B* **1995**, *51*, 7441−7450.
(37) Fujimori, A.; Saeki, M.; Kimizuka, N.; Taniguchi, M.; Suga, S. Photoemission Satellites and Electronic Structure of Fe_2O_3. *Phys. Rev. B* **1986**, *34*, 7318−7328.
(38) Li, S. Structural Design, Characterization, and Property Investigation of Iron Oxide Nanoparticles with Visible Light Photoactivity. Doctoral Thesis, Northeastern University, Shenyang, China, 2009.
(39) Marcus, R. A. Transfer Reactions in Chemistry: Theory and Experiment. *Pure Appl. Chem.* **1997**, *69*, 13−29.
(40) Sawada, H. An Electron Density Residual Study of α-Ferric Oxide. *Mater. Res. Bull.* **1996**, *31*, 141−146.
(41) Dräger, G.; Czolbe, W.; Leiro, J. A. High-Energy-Spectroscopy Studies of a Charge-Transfer Insulator: X-ray Spectra of α-Fe_2O_3. *Phys. Rev. B* **1992**, *45*, 8283−8287.